

# Fully Coupled Fluid-Structural Interactions Using an Efficient High Solution Upwind Scheme

Xiangying Chen\* and Ge-Cheng Zha†

Dept. of Mechanical and Aerospace Engineering

University of Miami

Coral Gables, Florida 33124

xychen@apollo.eng.miami.edu,

zha@apollo.eng.miami.edu

## Abstract

The E-CUSP upwind scheme recently developed by Zha and Hu is extended to moving grid system and is applied to calculate the flow induced vibration based on a fully coupled fluid-structure interaction methodology. The scheme is used to calculate the flow induced vibration of an elastically mounted cylinder, forced pitching airfoil, and an elastically mounted airfoil. The numerical results are compared with experimental data and have demonstrated the accuracy, efficiency and robustness of the new E-CUSP scheme for solving flow induced vibration problems with moving mesh systems.

## 1 Introduction

Flow induced structural vibration is one of the most critical technical problems affecting the reliability, cost and safety of aircraft. Due to the very complicated non-linear flow-structure interaction and multidisciplinary (fluid and structure) requirements, there is a lack of high accuracy and efficiency computational tools to study the basic physics and to predict the structural failure. The problems exist in both the airframe and aircraft engine systems.

There are generally two types of methods to calculate the fluid-structure interaction problems: the fluid and structure governing equations are loosely coupled or fully coupled. The loosely coupled model means that the structural response lags behind the flow field solution. This kind of methods may be limited to first-order accuracy in time regardless of the temporal accuracy of the individual solvers[1]. The fully coupled model is that the flow field and structure always respond simultaneously by exchanging the aerodynamic forcing and structural displacement within each iteration. Obviously, only the fully coupled model is rigorous in physical sense.

Recently, efforts have been made to develop the predicting capability for flow induced vibration. Bendiksen et al.[2] pioneered the research by using an explicit CFD code coupled with a structural

---

\* Post Doctoral Associate

† Associate Professor

integrator based on the convolution integral to obtain the flutter boundary for a NACA 64A010 airfoil. The loosely coupled model between the fluid and structural solvers include the work conducted by Guruswamy[3], Lee-Rausch et al.[4], Smith[5], Vermeersch et al.[6], Darracq, et. al [7], Blom et al.[8], Prananta et al.[9], and Bohbot et al.[10]. Alonso and Jameson developed a model which is close to the fully coupled method with the structural displacement updated every several fluid solver iterations[11]. The implicit Runge-Kutta method with multigrid acceleration is employed for the flow solver in Alonso’s work[11][12]. In 1997-98, Morton and Melville et al. developed a implicit fully coupled fluid structural interaction model, which used the Beam-Warming implicit scheme for the flow solver coupled with modal structural solver [13][14][1]. In 2000, Liu et al. developed a fully coupled method using Jameson’s explicit scheme with multigrid method and a finite element structural model [15].

Chen et al. recently have developed a fully coupled methodology for calculating the flow induced vibrations[16]. In their method, the Roe scheme is extended to moving grid system and is used with the finite-volume method. Unlike the central differencing used in[13][14][1], no artificial dissipation needs to be adjusted. The structure response is sensitive to different artificial dissipation. The unsteady solutions march in time by using a dual-time stepping implicit unfactored Gauss-Seidel iteration. The unsteady Navier-Stokes equations and the linear structural equations are fully coupled implicitly via successive iteration with pseudo time stepping. The moving/deforming mesh strategy is based on two mesh zones, a fine mesh zone surrounding the solid body without mesh deformation, and a coarse mesh zone surrounding the fine mesh zone and deforming with the solid object motion. This mesh deformation strategy can maintain the orthogonality of the mesh near the wall and save CPU time spent to re-mesh the grid near the solid wall.

However, the calculation based on fully coupled fluid-structure interaction is CPU expensive due to the intensive iterations between the fluid system and structure system. Hence, a numerical scheme that is CPU efficient and accurate is very desirable. The Roe scheme used in [16] for the flow field calculation consumes a lot of CPU time due to its matrix operation for the numerical dissipation. This paper is to employ a more CPU efficient scheme by avoiding the matrix operation to calculate the flow induced vibrations.

Recently, there are many efforts to develop efficient Riemann solvers using scalar dissipation instead of the matrix dissipation. For the scalar dissipation Riemann solver schemes, there are generally two types: H-CUSP schemes and E-CUSP schemes[17, 18, 19]. The abbreviation CUSP stands for “convective upwind and split pressure” named by Jameson[17, 18, 19]. The H-CUSP schemes have the total enthalpy from the energy equation in their convective vector, while the E-CUSP schemes use the total energy in the convective vector. The Liou’s AUSM family schemes, Van Leer-Hänel scheme[20], and Edwards’s LDFSS schemes[21, 22] belong to the H-CUSP group.

The H-CUSP schemes may have the advantage to better conserve the total enthalpy for steady state flows. However, from the characteristic theory point of view, the H-CUSP schemes are not fully consistent with the disturbance propagation directions, which may affect the stability and robustness of the schemes[23]. A H-CUSP scheme may have more inconsistency when it is extended to moving grid system. It will leave the pressure term multiplied by the grid velocity in the energy flux that can not be contained in the total enthalpy and the term has to be treated as a part of the pressure term. From characteristics point of view, it is not obvious how to treat this term in a consistent manner.

Recently, Zha and Hu suggested an efficient E-CUSP scheme which is consistent with the characteristic directions[23]. The scheme has low diffusion and is able to capture crisp shock profiles and

exact contact discontinuities. The scheme is shown to be accurate, robust and efficient since it only uses the scalar dissipation. In addition, it is fairly straightforward to extend the E-CUSP scheme of Zha-Hu to moving grid system. This is because the grid velocity belongs to the convective terms in the E-CUSP schemes. The pressure term is determined by the weighted average based on the wave eigenvalues from downstream and upstream. The Zha-Hu scheme is more efficient than the Roe scheme without matrix operation. For a 2D nozzle calculation, the CPU time to evaluate the flux using Zha-Hu scheme is only about 1/4 of that needed by the Roe scheme[23].

This paper is to apply the newly suggested E-CUSP scheme of Zha-Hu to a fully coupled fluid-structure interaction to achieve high efficiency and accuracy. The above methodology is proved to be robust, accurate and efficient by the computed flow induced vibration of an elastically mounted cylinder, a transonic pitching airfoil, and the elastically mounted NACA 64A010 airfoil.

## 2 CFD Aerodynamic Model

### 2.1 Flow Governing Equations

The governing equations for the flow field computation are the Reynolds-Averaged Navier-Stokes equations (RANS) with Favre mass average which can be transformed to the generalized coordinates and expressed as:

$$\frac{\partial \mathbf{Q}'}{\partial t} + \frac{\partial \mathbf{E}'}{\partial \xi} + \frac{\partial \mathbf{F}'}{\partial \eta} + \frac{\partial \mathbf{G}'}{\partial \zeta} = \frac{1}{Re} \left( \frac{\partial \mathbf{E}'_{\mathbf{v}}}{\partial \xi} + \frac{\partial \mathbf{F}'_{\mathbf{v}}}{\partial \eta} + \frac{\partial \mathbf{G}'_{\mathbf{v}}}{\partial \zeta} \right) \quad (1)$$

where  $Re$  is Reynolds number and

$$\mathbf{Q}' = \frac{\mathbf{Q}}{J} \quad (2)$$

$$\mathbf{E}' = \frac{1}{J}(\xi_t \mathbf{Q} + \xi_x \mathbf{E} + \xi_y \mathbf{F} + \xi_z \mathbf{G}) = \frac{1}{J}(\xi_t \mathbf{Q} + \mathbf{E}'') \quad (3)$$

$$\mathbf{F}' = \frac{1}{J}(\eta_t \mathbf{Q} + \eta_x \mathbf{E} + \eta_y \mathbf{F} + \eta_z \mathbf{G}) = \frac{1}{J}(\eta_t \mathbf{Q} + \mathbf{F}'') \quad (4)$$

$$\mathbf{G}' = \frac{1}{J}(\zeta_t \mathbf{Q} + \zeta_x \mathbf{E} + \zeta_y \mathbf{F} + \zeta_z \mathbf{G}) = \frac{1}{J}(\zeta_t \mathbf{Q} + \mathbf{G}'') \quad (5)$$

$$\mathbf{E}'_{\mathbf{v}} = \frac{1}{J}(\xi_x \mathbf{E}_{\mathbf{v}} + \xi_y \mathbf{F}_{\mathbf{v}} + \xi_z \mathbf{G}_{\mathbf{v}}) \quad (6)$$

$$\mathbf{F}'_{\mathbf{v}} = \frac{1}{J}(\eta_x \mathbf{E}_{\mathbf{v}} + \eta_y \mathbf{F}_{\mathbf{v}} + \eta_z \mathbf{G}_{\mathbf{v}}) \quad (7)$$

$$\mathbf{G}'_{\mathbf{v}} = \frac{1}{J}(\zeta_x \mathbf{E}_{\mathbf{v}} + \zeta_y \mathbf{F}_{\mathbf{v}} + \zeta_z \mathbf{G}_{\mathbf{v}}) \quad (8)$$

where the variable vector  $\mathbf{Q}$ , and inviscid flux vectors  $\mathbf{E}$ ,  $\mathbf{F}$ , and  $\mathbf{G}$  are

$$\mathbf{Q} = \begin{pmatrix} \bar{\rho} \\ \bar{\rho}\tilde{u} \\ \bar{\rho}\tilde{v} \\ \bar{\rho}\tilde{w} \\ \bar{\rho}\tilde{e} \end{pmatrix}, \mathbf{E} = \begin{pmatrix} \bar{\rho}\tilde{u} \\ \bar{\rho}\tilde{u}\tilde{u} + \tilde{p} \\ \bar{\rho}\tilde{u}\tilde{v} \\ \bar{\rho}\tilde{u}\tilde{w} \\ (\bar{\rho}\tilde{e} + \tilde{p})\tilde{u} \end{pmatrix}, \mathbf{F} = \begin{pmatrix} \bar{\rho}\tilde{v} \\ \bar{\rho}\tilde{u}\tilde{v} \\ \bar{\rho}\tilde{v}\tilde{v} + \tilde{p} \\ \bar{\rho}\tilde{w}\tilde{v} \\ (\bar{\rho}\tilde{e} + \tilde{p})\tilde{v} \end{pmatrix}, \mathbf{G} = \begin{pmatrix} \bar{\rho}\tilde{w} \\ \bar{\rho}\tilde{u}\tilde{w} \\ \bar{\rho}\tilde{v}\tilde{w} \\ \bar{\rho}\tilde{w}\tilde{w} + \tilde{p} \\ (\bar{\rho}\tilde{e} + \tilde{p})\tilde{w} \end{pmatrix},$$

The  $\mathbf{E}''$ ,  $\mathbf{F}''$ , and  $\mathbf{G}''$  are the inviscid fluxes at the stationary grid system and are expressed as:

$$\mathbf{E}'' = \xi_x \mathbf{E} + \xi_y \mathbf{F} + \xi_z \mathbf{G},$$

$$\mathbf{F}'' = \eta_x \mathbf{E} + \eta_y \mathbf{F} + \eta_z \mathbf{G},$$

$$\mathbf{G}'' = \zeta_x \mathbf{E} + \zeta_y \mathbf{F} + \zeta_z \mathbf{G},$$

and the viscous flux vectors are given by

$$\mathbf{E}_{\mathbf{v}} = \begin{pmatrix} 0 \\ \bar{\tau}_{xx} - \frac{\rho u'' u''}{Q_x} \\ \bar{\tau}_{xy} - \frac{\rho u'' v''}{Q_x} \\ \bar{\tau}_{xz} - \frac{\rho u'' w''}{Q_x} \\ Q_x \end{pmatrix}, \mathbf{F}_{\mathbf{v}} = \begin{pmatrix} 0 \\ \bar{\tau}_{yx} - \frac{\rho v'' u''}{Q_y} \\ \bar{\tau}_{yy} - \frac{\rho v'' v''}{Q_y} \\ \bar{\tau}_{yz} - \frac{\rho v'' w''}{Q_y} \\ Q_y \end{pmatrix}, \mathbf{G}_{\mathbf{v}} = \begin{pmatrix} 0 \\ \bar{\tau}_{zx} - \frac{\rho w'' u''}{Q_z} \\ \bar{\tau}_{zy} - \frac{\rho w'' v''}{Q_z} \\ \bar{\tau}_{zz} - \frac{\rho w'' w''}{Q_z} \\ Q_z \end{pmatrix}$$

In above equations,  $\rho$  is the density,  $u, v$ , and  $w$  are the Cartesian velocity components in  $x, y$  and  $z$  directions,  $p$  is the static pressure, and  $e$  is the total energy per unit mass. The overbar denotes the Reynolds-averaged quantity, tilde and double-prime denote the Favre mean and Favre fluctuating part of the turbulent motion respectively. All the flow variables in above equations are non-dimensionalized by using the freestream quantities and reference length  $L$ .

Let subscript 1, 2 and 3 represent the coordinates,  $x, y$ , and  $z$ , and use Einstein summation convention, the shear-stress and  $Q_x, Q_y, Q_z$  terms in non-dimensional forms can be expressed in tensor form as

$$\bar{\tau}_{ij} = -\frac{2}{3}\tilde{\mu}\frac{\partial\tilde{u}_k}{\partial x_k}\delta_{ij} + \tilde{\mu}\left(\frac{\partial\tilde{u}_i}{\partial x_j} + \frac{\partial\tilde{u}_j}{\partial x_i}\right) \quad (9)$$

$$Q_i = \tilde{u}_j(\bar{\tau}_{ij} - \overline{\rho u_i'' u_j''}) - (\bar{q}_i + C_p \overline{\rho T'' u_i''}) \quad (10)$$

where the mean molecular heat flux is

$$\bar{q}_i = -\frac{\tilde{\mu}}{(\gamma - 1)Pr} \frac{\partial a^2}{\partial x_i} \quad (11)$$

The molecular viscosity  $\tilde{\mu} = \tilde{\mu}(\tilde{T})$  is determined by Sutherland law, and  $a = \sqrt{\gamma RT_\infty}$  is the speed of sound. The equation of state closes the system,

$$\bar{\rho}\tilde{e} = \frac{\tilde{p}}{(\gamma - 1)} + \frac{1}{2}\bar{\rho}(\tilde{u}^2 + \tilde{v}^2 + \tilde{w}^2) + k \quad (12)$$

where  $\gamma$  is the ratio of specific heats,  $k$  is the Favre mass-averaged turbulence kinetic energy. The turbulent shear stresses and heat flux appeared in above equations are calculated by Baldwin-Lomax model[24]. An additional equation is solved to enforce the geometry conservation law[16].

## 2.2 Time Marching Scheme

The time dependent governing equation (1) is solved using the control volume method with the concept of dual time stepping suggested by Jameson[25]. A pseudo temporal term  $\frac{\partial \mathbf{Q}}{\partial \tau}$  is added to the governing equation (1). This term vanishes at the end of each physical time step, and has no influence on the accuracy of the solution. However, instead of using the explicit scheme as in [25], an implicit pseudo time marching scheme using Gauss-Seidel iteration is employed to achieve high CPU efficiency. For unsteady time accurate computations, the temporal term is discretized implicitly using a three point, backward differencing as the following

$$\frac{\partial \mathbf{Q}}{\partial t} = \frac{3Q^{n+1} - 4Q^n + Q^{n-1}}{2\Delta t} \quad (13)$$

where  $n$  is the time level index. The pseudo temporal term is discretized with first order Euler scheme. Let  $m$  stand for the iteration index within a physical time step, the semi-discretized governing equation (1) can be expressed as

$$\left[\left(\frac{1}{\Delta \tau} + \frac{1.5}{\Delta t}\right)I - \left(\frac{\partial R}{\partial Q}\right)^{n+1,m}\right]\delta Q^{n+1,m+1} = R^{n+1,m} - \frac{3Q^{n+1,m} - 4Q^n + Q^{n-1}}{2\Delta t} \quad (14)$$

where the  $\Delta \tau$  is the pseudo time step,  $R$  is the net flux going through the control volume,

$$R = -\frac{1}{V} \int_{\mathbf{s}} [(F - F_v)\mathbf{i} + (G - G_v)\mathbf{j} + (H - H_v)\mathbf{k}] \cdot d\mathbf{s} \quad (15)$$

where  $V$  is the volume of the control volume,  $\mathbf{s}$  is the control volume surface area vector. Equation (14) is solved using the unfactored Gauss-Seidel iteration. The method is unconditionally stable and can reach very large pseudo time step since no factorization error is introduced.

## 2.3 The Zha-Hu E-CUSP Scheme in Moving Mesh System

To clearly describe the formulations, the vectors of  $\mathbf{Q}$  and  $\mathbf{E}'$  in Equation (3) are given below:

$$\mathbf{Q} = \begin{pmatrix} \bar{\rho} \\ \bar{\rho}\tilde{u} \\ \bar{\rho}\tilde{v} \\ \bar{\rho}\tilde{w} \\ \bar{\rho}\tilde{e} \end{pmatrix}, \quad \mathbf{E}' = \frac{1}{J}\hat{\mathbf{E}}, \quad \hat{\mathbf{E}} = \begin{pmatrix} \bar{\rho}\tilde{U} \\ \bar{\rho}\tilde{u}\tilde{U} + \xi_x\tilde{p} \\ \bar{\rho}\tilde{v}\tilde{U} + \xi_y\tilde{p} \\ \bar{\rho}\tilde{w}\tilde{U} + \xi_z\tilde{p} \\ \bar{\rho}\tilde{e}\tilde{U} + \tilde{p}\tilde{U} \end{pmatrix} \quad (16)$$

$\tilde{U}$  is the contravariant velocity in  $\xi$  direction defined as the following:

$$\tilde{U} = \xi_t + \xi_x\tilde{u} + \xi_y\tilde{v} + \xi_z\tilde{w} \quad (17)$$

We define  $\bar{U}$  as:

$$\bar{U} = \tilde{U} - \xi_t \quad (18)$$

The Jacobian matrix  $\hat{\mathbf{A}}$  is defined as

$$\hat{\mathbf{A}} = \frac{\partial \hat{\mathbf{E}}}{\partial \mathbf{Q}} = \hat{\mathbf{T}} \hat{\mathbf{\Lambda}} \hat{\mathbf{T}}^{-1} \quad (19)$$

where  $\hat{\mathbf{T}}$  is the right eigenvector matrix of  $\hat{\mathbf{A}}$ , and  $\hat{\mathbf{\Lambda}}$  is the eigenvalue matrix of  $\hat{\mathbf{A}}$  on moving grid system with the eigenvalues of

$$(\tilde{U} + \tilde{C}, \tilde{U} - \tilde{C}, \tilde{U}, \tilde{U}, \tilde{U}) \quad (20)$$

where  $\tilde{C}$  is the speed of sound corresponding to the contravariant velocity:

$$\tilde{C} = c \sqrt{\xi_x^2 + \xi_y^2 + \xi_z^2} \quad (21)$$

where  $c = \sqrt{\gamma RT}$  is the physical speed of sound.

Due to the homogeneous relationship between  $\mathbf{Q}$  and  $\hat{\mathbf{E}}$ , the following formulation applies:

$$\hat{\mathbf{E}} = \hat{\mathbf{A}} \mathbf{Q} = \hat{\mathbf{T}} \hat{\mathbf{\Lambda}} \hat{\mathbf{T}}^{-1} \mathbf{Q} \quad (22)$$

In an E-CUSP scheme, the eigenvalue matrix is split as the following:

$$\hat{\mathbf{A}} = \begin{pmatrix} \tilde{U} - \tilde{C} & 0 & 0 & 0 & 0 \\ 0 & \tilde{U} & 0 & 0 & 0 \\ 0 & 0 & \tilde{U} & 0 & 0 \\ 0 & 0 & 0 & \tilde{U} & 0 \\ 0 & 0 & 0 & 0 & \tilde{U} + \tilde{C} \end{pmatrix} = \tilde{U} [\mathbf{I}] + \begin{pmatrix} -\tilde{C} & 0 & 0 & 0 & 0 \\ 0 & 0 & 0 & 0 & 0 \\ 0 & 0 & 0 & 0 & 0 \\ 0 & 0 & 0 & 0 & 0 \\ 0 & 0 & 0 & 0 & \tilde{C} \end{pmatrix} \quad (23)$$

Obviously the grid velocity term  $\xi_t [\mathbf{I}]$  due to the moving mesh is naturally included in the convective term,  $\tilde{U}$ , as given in eq.(17). Therefore, Equation (22) becomes

$$\hat{\mathbf{E}} = [\tilde{U} [\mathbf{I}] + \begin{pmatrix} -\tilde{C} & 0 & 0 & 0 & 0 \\ 0 & 0 & 0 & 0 & 0 \\ 0 & 0 & 0 & 0 & 0 \\ 0 & 0 & 0 & 0 & 0 \\ 0 & 0 & 0 & 0 & \tilde{C} \end{pmatrix}] \mathbf{Q} = \hat{\mathbf{E}}^c + \hat{\mathbf{E}}^p = \begin{pmatrix} \bar{\rho} \tilde{U} \\ \bar{\rho} \tilde{u} \tilde{U} \\ \bar{\rho} \tilde{v} \tilde{U} \\ \bar{\rho} \tilde{w} \tilde{U} \\ \bar{\rho} \tilde{e} \tilde{U} \end{pmatrix} + \begin{pmatrix} 0 \\ \xi_x \tilde{p} \\ \xi_y \tilde{p} \\ \xi_z \tilde{p} \\ \tilde{p} \tilde{U} \end{pmatrix} \quad (24)$$

where  $\hat{\mathbf{E}}^c$  and  $\hat{\mathbf{E}}^p$  are namely convective and pressure fluxes. As shown above, the way of breaking up the total flux into convective and pressure fluxes in E-CUSP type is purely based on the analysis of characteristics of the system. As shown in eq. (24), the convective flux has the upwind characteristic  $\tilde{U}$  and it is only associated with the convective velocity. The pressure flux has a downwind and upwind characteristic and it totally depends on the propagation of acoustic wave.

The E-CUSP scheme of Zha-Hu[23] can be extended to moving mesh system as the following:

$$\hat{\mathbf{E}}_{\frac{1}{2}} = \frac{1}{2}[(\bar{\rho}\tilde{U})_{\frac{1}{2}}(\mathbf{q}^c_L + \mathbf{q}^c_R) - |\bar{\rho}\tilde{U}|_{\frac{1}{2}}(\mathbf{q}^c_R - \mathbf{q}^c_L)] + \begin{pmatrix} 0 \\ \mathcal{P}^+ \tilde{p}\xi_x \\ \mathcal{P}^+ \tilde{p}\xi_y \\ \mathcal{P}^+ \tilde{p}\xi_z \\ \frac{1}{2}\tilde{p}(\tilde{U} + \tilde{C}_{\frac{1}{2}}) \end{pmatrix}_L + \begin{pmatrix} 0 \\ \mathcal{P}^- \tilde{p}\xi_x \\ \mathcal{P}^- \tilde{p}\xi_y \\ \mathcal{P}^- \tilde{p}\xi_z \\ \frac{1}{2}\tilde{p}(\tilde{U} - \tilde{C}_{\frac{1}{2}}) \end{pmatrix}_R \quad (25)$$

where

$$(\bar{\rho}\tilde{U})_{\frac{1}{2}} = (\bar{\rho}_L\tilde{U}_L^+ + \bar{\rho}_R\tilde{U}_R^-) \quad (26)$$

$$\mathbf{q}^c = \begin{pmatrix} 1 \\ \tilde{u} \\ \tilde{v} \\ \tilde{w} \\ \tilde{e} \end{pmatrix} \quad (27)$$

$$\tilde{C}_{\frac{1}{2}} = \frac{1}{2}(\tilde{C}_L + \tilde{C}_R) \quad (28)$$

$$\tilde{M}_L = \frac{\tilde{U}_L}{\tilde{C}_{\frac{1}{2}}}, \quad \tilde{M}_R = \frac{\tilde{U}_R}{\tilde{C}_{\frac{1}{2}}} \quad (29)$$

$$\tilde{U}_L^+ = \tilde{C}_{\frac{1}{2}} \left\{ \frac{\tilde{M}_L + |\tilde{M}_L|}{2} + \alpha_L \left[ \frac{1}{4}(\tilde{M}_L + 1)^2 - \frac{\tilde{M}_L + |\tilde{M}_L|}{2} \right] \right\} \quad (30)$$

$$\tilde{U}_R^- = \tilde{C}_{\frac{1}{2}} \left\{ \frac{\tilde{M}_R - |\tilde{M}_R|}{2} + \alpha_R \left[ -\frac{1}{4}(\tilde{M}_R - 1)^2 - \frac{\tilde{M}_R - |\tilde{M}_R|}{2} \right] \right\} \quad (31)$$

$$\alpha_L = \frac{2(\tilde{p}/\bar{\rho})_L}{(\tilde{p}/\bar{\rho})_L + (\tilde{p}/\bar{\rho})_R}, \quad \alpha_R = \frac{2(\tilde{p}/\bar{\rho})_R}{(\tilde{p}/\bar{\rho})_L + (\tilde{p}/\bar{\rho})_R} \quad (32)$$

$$\mathcal{P}^{\pm} = \frac{1}{4}(\tilde{M} \pm 1)^2(2 \mp \tilde{M}) \pm \alpha \tilde{M}(\tilde{M}^2 - 1)^2, \quad \alpha = \frac{3}{16} \quad (33)$$

$$\bar{C} = \tilde{C} - \xi_t \quad (34)$$

$$\bar{C}_{\frac{1}{2}} = \frac{1}{2}(\bar{C}_L + \bar{C}_R) \quad (35)$$

Please note that, in the energy equation of the pressure splitting,  $\tilde{U}$  and  $\tilde{C}$  are used instead of  $\bar{U}$  and  $\bar{C}$ .  $\bar{C}$  is constructed taking into account the effect of the grid speed so that the flux will

transit from subsonic to supersonic smoothly. When  $\xi_t = 0$ , eq. (25) naturally returns to the one for stationary grid.

For supersonic flow,

$$\text{when } \tilde{U}_L \geq \tilde{C}, \hat{\mathbf{E}}_{\frac{1}{2}} = \hat{\mathbf{E}}_L$$

$$\text{when } \tilde{U}_R \leq -\tilde{C}, \hat{\mathbf{E}}_{\frac{1}{2}} = \hat{\mathbf{E}}_R$$

## 2.4 Boundary Conditions

The flow field is solved subject to appropriate boundary conditions described as bellow:

(1) Upstream boundary condition: The outer boundary is divided into upstream and downstream boundaries according to whether the direction of its segment is toward or backward to the ambient flow direction. On upstream boundary, it is assumed that the streamwise velocity  $u$  is uniform, and transverse velocity  $v = 0$ . Other primitive variables are specified according to the freestream condition except the pressure which is extrapolated from interior.

(2) Downstream boundary condition: All the flow quantities are extrapolated from interior except the pressure which is set to be its freestream value.

(3) Solid wall boundary condition: At moving boundary surface, the no-slip condition is enforced by extrapolating the velocity between the phantom and interior cells,

$$u_0 = 2\dot{x}_b - u_1, \quad v_0 = 2\dot{y}_b - v_1 \quad (36)$$

where  $u_0$  and  $v_0$  denote the velocity at phantom cell,  $u_1$  and  $v_1$  denote the velocity at the 1st interior cell close to the boundary, and  $u_b$  and  $v_b$  are the velocity on the moving boundary.

The other two conditions to be imposed on the solid wall are the adiabatic wall condition and the inviscid normal momentum equation[13] as follows,

$$\frac{\partial T}{\partial \eta} = 0, \quad \frac{\partial p}{\partial \eta} = - \left( \frac{\rho}{\eta_x^2 + \eta_y^2} \right) (\eta_x \ddot{x}_b + \eta_y \ddot{y}_b) \quad (37)$$

## 3 Structural Models

### 3.1 Elastically Mounted Cylinder

For the computations of the vortex-induced oscillating cylinder, which is elastically supported as shown in Figure 1 so that it oscillates only in the direction aligned with or normal to the incoming flow, the structural dynamic equations which governs the motion of the cylinder are:

$$m\ddot{x} + C_x\dot{x} + K_x x = D \quad (38)$$

$$m\ddot{y} + C_y\dot{y} + K_y y = L \quad (39)$$

These equations are solved implicitly together with the equations of flow motion, Equation (14) in a fully coupled manner. In Equation (38),  $\ddot{x}$ ,  $\dot{x}$ , and  $x$  represent the dimensionless horizontal



acceleration, velocity and displacement of the moving object respectively. Similarly,  $\ddot{y}$ ,  $\dot{y}$ , and  $y$  in Equation (39) represent their corresponding ones in vertical direction.  $m$ ,  $L$ , and  $D$  are the mass, lift, and drag per unit span respectively,  $C_x$  and  $C_y$  are the damping coefficients in horizontal and vertical directions,  $K_x$  and  $K_y$  are the spring constants in horizontal and vertical directions. In present study, this 'self-excited oscillators' is assumed to have the same response in both direction, i.e.  $C_x = C_y$  and  $K_x = K_y$ .

If the normalization procedure is applied to Equations (38) and (39) by using the same reference scales of those used for the equations of flow motion, the following nondimensional equations are obtained

$$\ddot{x} + 2\zeta \left(\frac{2}{\bar{u}}\right) \dot{x} + \left(\frac{2}{\bar{u}}\right)^2 x = \frac{2}{\mu_s \pi} C_d \quad (40)$$

$$\ddot{y} + 2\zeta \left(\frac{2}{\bar{u}}\right) \dot{y} + \left(\frac{2}{\bar{u}}\right)^2 y = \frac{2}{\mu_s \pi} C_l \quad (41)$$

where  $\zeta$  is the nondimensional structural damping coefficient calculated by  $\zeta = \frac{C_{x,y}}{2\sqrt{mK_{x,y}}}$ ,  $\bar{u}$  is the reduced velocity defined by  $\bar{u} = \frac{U_\infty}{b\omega}$ ,  $b$  is radius of the cylinder,  $\omega = \sqrt{K_{x,y}/m}$ , the mass ratio,  $\mu_s = \frac{m}{\pi\rho_\infty b^2}$ ,  $C_d$  and  $C_l$  are the drag and lift force coefficients respectively. Then the equations are transformed to a matrix form and expressed by

$$[\mathbf{M}] \frac{\partial \{\mathbf{S}\}}{\partial t} + [\mathbf{K}] \{\mathbf{S}\} = \mathbf{q} \quad (42)$$

where

$$\mathbf{S} = \begin{pmatrix} x \\ \dot{x} \\ y \\ \dot{y} \end{pmatrix}, \mathbf{M} = [I], \mathbf{K} = \begin{pmatrix} 0 & -1 & 0 & 0 \\ \left(\frac{2}{\bar{u}}\right)^2 & 2\zeta \left(\frac{2}{\bar{u}}\right) & 0 & 0 \\ 0 & 0 & 0 & -1 \\ 0 & 0 & \left(\frac{2}{\bar{u}}\right)^2 & 2\zeta \left(\frac{2}{\bar{u}}\right) \end{pmatrix}, \mathbf{q} = \begin{pmatrix} 0 \\ \frac{2}{\mu_s \pi} C_d \\ 0 \\ \frac{2}{\mu_s \pi} C_l \end{pmatrix}.$$

To couple the structural equations with the equations of flow motion and solve them implicitly in each physical time step, above equations are discretized and integrated in a manner consistent with Equation (14) to yield

$$\left( \frac{1}{\Delta\tau} \mathbf{I} + \frac{1.5}{\Delta t} \mathbf{M} + \mathbf{K} \right) \delta \mathbf{S}^{n+1,m+1} = -\mathbf{M} \frac{3\mathbf{S}^{n+1,m} - 4\mathbf{S}^n + \mathbf{S}^{n-1}}{2\Delta t} - \mathbf{K} \mathbf{S}^{n+1,m} + \mathbf{q}^{n+1,m+1} \quad (43)$$

where  $n$  is the physical time level index while  $m$  stands for the pseudo time index. The detailed coupling procedure between the fluid and structural systems is given in section 4.

### 3.2 Elastically Mounted Airfoil

Unlike the structural model of the vortex-induced oscillating cylinder, the system of the elastically mounted airfoil is assumed to be undamped. The airfoil is allowed to move in pitch about a given elastic axis and plunge vertically. The pitch axis is defined by a distance  $a$ , which is the multiple

of the semi-chord length with the origin point located at the mid-chord position. If  $a$  is positive, it means the axis is located downstream of the mid-chord, negative means being located upstream of the mid-chord point.

A sketch of the elastically mounted airfoil is depicted in Figure 2. The motion of such an elastic system can be described by using the following equations

$$m\ddot{h} + S_\alpha\ddot{\alpha} + K_h h = -L \quad (44)$$

$$S_\alpha\ddot{h} + I_\alpha\ddot{\alpha} + K_\alpha\alpha = M \quad (45)$$

where  $h$  and  $\alpha$  are the plunging and pitching displacements respectively,  $m$  is the mass per unit span,  $S_\alpha$  is the static moment around the elastic axis,  $I_\alpha$  is the rotational moment of inertia,  $K_h$  and  $K_\alpha$  are plunging and pitching spring constants respectively,  $L$  is the lift force and  $M$  is the moment around the elastic axis. The equations of the structure motion (44) and (45) are normalized by using semi-chord  $b$  as the length dimension, the uncoupled natural frequency in pitch  $\omega_\alpha$  as the time scale, and are expressed as

$$\ddot{h} + x_\alpha\ddot{\alpha} + \left(\frac{\omega_h}{\omega_\alpha}\right)^2 h = -\frac{U^{*2}}{\mu\pi}C_l \quad (46)$$

$$x_\alpha\ddot{h} + r_\alpha^2\ddot{\alpha} + r_\alpha^2\alpha = \frac{U^{*2}}{\mu\pi}C_m \quad (47)$$

where  $x_\alpha$  is the static unbalance,  $\omega_h$  is the uncoupled natural frequency in plunge,  $r_\alpha^2$  is the squared radius of gyration,  $U^*$  is the reduced velocity defined as  $\frac{U_\infty}{\omega_\alpha b}$ ,  $C_l$  and  $C_m$  are the lift and moment coefficient respectively. Since the time scale used in Equations (46) and (47) is different from the one used in the governing equations of flow, the structural dimensionless time  $t_s^*$  needs to be re-scaled and keep its consistency with the entire system during the computation, i.e.,  $t_s^* = \frac{\omega_\alpha L}{U_\infty} t_f^*$ , where  $t_f^*$  is the dimensionless time for flow and the  $L$  is the length scale. Finally the equations are cast into the form of Equations (42) and (43), and the corresponding matrices are

$$\mathbf{S} = \begin{pmatrix} h \\ \dot{h} \\ \alpha \\ \dot{\alpha} \end{pmatrix}, \mathbf{M} = \begin{pmatrix} 1 & 0 & 0 & 0 \\ 0 & 1 & 0 & x_\alpha \\ 0 & 0 & 1 & 0 \\ 0 & x_\alpha & 0 & r_\alpha^2 \end{pmatrix}, \mathbf{K} = \begin{pmatrix} 0 & -1 & 0 & 0 \\ \left(\frac{\omega_h}{\omega_\alpha}\right)^2 & 0 & 0 & 0 \\ 0 & 0 & 0 & -1 \\ 0 & 0 & r_\alpha^2 & 0 \end{pmatrix}, \mathbf{q} = \begin{pmatrix} 0 \\ -\frac{U^{*2}}{\mu\pi}C_l \\ 0 \\ \frac{U^{*2}}{\mu\pi}C_m \end{pmatrix}.$$

## 4 Flow-Structure Coupling

Within a physical time step, the structural motion and the flow field are unknown and are solved iteratively between the fluid and structural systems in a fully couple manner. The following is the procedure:

(1) The variables at new time level  $n + 1$  of the flow and structural equations initially are set to the values of time level  $n$ .

(2) Calculate the aerodynamic forces including lift, drag, and torque exerting on the solid body of the object.

(3) Determine the position of the moving object subject to the aerodynamic forces by solving the structural equations.

(4) Re-generate the mesh and calculate the grid velocity at each node point according to the updated structural position.

(5) Calculate the flow field by solving the equations of flow motion for the updated mesh and structural position.

(6) Check the maximum residuals for both solutions of the flow and the structural equations. If the maximum residuals are greater than the prescribed convergence criteria, go back to step (2) and proceed to the next pseudo time level  $m + 1$ , otherwise the flow field and the movement of the moving object are determined and go back to step (1) to start the next new physical time step  $n + 1$ . The procedure can be also seen in the flow chart given in Figure 3.

## 5 Results and Discussion

Presented in this section are the numerical results of the vortex-induced oscillating cylinder, the forced pitching NACA 64A010 airfoil, and the flow-induced vibration of a NACA 64A010 airfoil.

### 5.1 Elastically Mounted Cylinder

#### 5.1.1 Stationary Cylinder

The flow past a stationary cylinder is used as an unsteady flow validation case. The fine mesh zone mentioned in the previous section is shown in Figure 4. The baseline mesh dimensions are  $120 \times 80$  in circumferential and radial directions. The far field boundary is located 20 diameters away from the center of the cylinder. The Reynolds number based on the free-stream condition and cylinder diameter is,  $Re = 500$ . The laminar Navier-Stokes equations will be solved due to the low Reynolds number.

The computed drag and lift coefficients are shown in Figure 5. As shown in the figure, the lift oscillates at certain frequency in terms of the Strouhal number. The drag coefficient oscillates with twice that frequency. The mesh refinement study and computed Strouhal number, drag, lift and moment coefficients are listed in Table 1

Table 1: Results of Mesh Refinement Study and comparison with the experiments

Mesh Dimension	$St_{C_d}$	$St_{C_l}$	$St_{C_m}$	$C_l$	$C_d$
120×80	0.4395	0.2197	0.2197	±1.1810	1.4529±0.1305
200×120	0.4516	0.2246	0.2246	±1.2267	1.4840±0.1450
(Roshko 1954[26])		0.2075			
(Goldstein 1938[27])		0.2066			
384×96 (Alonso 1995[12])	0.46735	0.23313		1.14946( $C_{lmax}$ )	1.31523( $C_{davg}$ )

Table 1 shows that the solution is converged based on mesh size. The computed lift frequency by Zha-Hu CUSP scheme agrees well with the experimental results of Roshko[28] and Goldstein[27],

and is closer to the experimental results than the one computed by by Alonso et al.[12], which uses larger size of grid points.

## 5.2 Vortex-Induced Oscillating Cylinder

After validating the stationary cylinder vortex shedding flow, the cylinder is released to be controlled by the structure model as shown in Figure 1. The corresponding structural equations are given in section 3.1. The laminar Navier-Stokes equations are solved due to the low Reynolds number,  $Re = 500$ .

Using the temporally periodic solution obtained in the computation of stationary cylinder as the initial flow field, the computation is resumed after the cylinder is let to move in both streamwise and transverse directions. For the purpose of comparison with the experimental data of Griffin[29] several different combinations of structural parameters are used in the computations.

Morton et al.[13] suggested to use the reduced velocity  $\bar{u} = \frac{1}{\pi St}$  such that the structural oscillator works under or near the resonance conditions. Therefore the computed  $St$  number from the stationary cylinder is used to determine  $\bar{u}$ . For all the cases of oscillating cylinder,  $St$  is set to be 0.2, corresponding to  $\bar{u} = 1.5915$ . Different mass ratios,  $\mu_s$ , are used to test the different responses of the structural system. They are equal to 1.2732, 5.0, and 12.7324 respectively. To match the wide range of the experimental data, the damping ratio,  $\zeta$ , is chosen from the range between 0.001 - 1.583.

The dimensionless physical time step  $\Delta t = 0.05$  is used, which corresponds to approximately 100 time steps per period determined by the Strouhal number used. The CFL number for the pseudo time steps varies from case to case. For the large cylinder movement cases, smaller pseudo time steps are used to limit the displacement of the cylinder during each iteration.

For the cases computed, the CFL number varies from 5 to 500. The iteration number within one physical time step varies from 20 to 100. Fig. 6 shows a typical iteration history within one physical time step. Both the residual of the CFD solver and structure are reduced to machine zero. The structure solver usually converges faster than the CFD solver.

Figure 7 displays the computed vorticity contours around the oscillating cylinder. It shows how the vortexes are shed at the moment when the cylinder bounds back toward its mean position in  $y$  direction.

A typical trajectory of the center position of the moving cylinder is plotted in Figure 8, which is similar to the results computed by Blackburn et al.[30] and Alonso et al.[12]

All the numerical results for present study are plotted in Figure 9 for the three values of  $\mu_s$ . Also plotted are the computations of Alonso et al. [12] with  $\mu_s = 5.0$ , computations of Morton et al.[13] with  $\mu_s = 12.73$ , and the experimental data of Griffin[29]. In the figure, the abscissa is the reduced damping with the form of  $8\pi^2 St^2 \zeta \frac{m}{\rho D^2}$  [30], and the ordinate is the cross-flow displacement of motion normalized by the diameter of the cylinder. Overall, very good agreement is observed between the present results and the experimental results, especially for the case of  $\mu_s = 1.2732$ . The figure shows that the higher values of mass ratios ( $\mu_s = 5.0$  and  $\mu_s = 12.7324$ ) give less satisfactory results than those with  $\mu_s = 1.2732$ , particularly at low damping ratios. However, they agree well with the results of Morton et al.[13] ( $\mu_s = 12.73$ ).

### 5.3 Elastically Mounted Airfoil

#### 5.3.1 Steady State Transonic Airfoil

As the validation of the Zha-Hu CUSP scheme for transonic airfoils, the steady state solution of the transonic RAE 2822 airfoil is calculated first. The freestream condition for this study are listed in Table 2 below.

Table 2: Free-stream condition for RAE 2822 Airfoil

Mach number	Static Pressure (psia)	Temperature (R)	Angle-of-Attack (deg)	Reynolds Number
0.729	15.8073	460.0	2.31	$6.5 \times 10^6$

The turbulent Reynolds stress and heat flux is calculated by the Baldwin-Lomax algebraic model[24]. This case is run using an O-type grid with three different dimensions, they are  $128 \times 50 \times 1$ ,  $256 \times 55 \times 1$ , and  $512 \times 95 \times 1$  respectively. The outer boundary extends to 15 chords from the center of the airfoil. The experimental data provided by Cook et al.[31] are available for validation. The comparison of pressure coefficient on the airfoil is shown in Figure 10. Overall, very good agreement is obtained between the computation and experiment for each mesh dimension, especially for the two larger ones which appear to be sufficient to capture the shock on the suction surface of the airfoil without using any limiter. The important aerodynamic coefficients from both simulation and experiment are summarized in Table 3.

Table 3: Aerodynamic coefficients and  $y+$  for RAE 2822 Airfoil

Mesh Dimension	$C_d$	$C_l$	$C_m$	$y+$
$128 \times 50$	0.01482	0.73991	0.09914	0.0833 - 2.3864
$256 \times 55$	0.01455	0.73729	0.09840	0.1318 - 2.4016
$512 \times 95$	0.01426	0.74791	0.09994	0.2309 - 2.0228
Prananta et al.[9]	0.01500	0.74800	0.09800	
Experiment	0.01270	0.74300	0.09500	

It can be seen in Table 3 that the predicted lift coefficients with all mesh dimensions agree well with the experiment. The computed drag and moment coefficients show larger errors, but they have the similar accuracy as those computed by Prananta et al.[9]. The relatively large error of the drag and moment may be mostly due to the inadequacy of the turbulence model, which is difficult to predict the surface friction accurately.

#### 5.3.2 Forced Pitching Airfoil

As a validation case of the scheme for moving grid system, the forced pitching NACA 64A010 airfoil is calculated. For this transonic airfoil, the Reynolds averaged Navier-Stokes equations with Baldwin-Lomax turbulence model are solved. Similar to the previous computation of the flow over

the stationary airfoil, an O-type mesh consisting of  $280 \times 65$  cells is employed for the computations of forced pitching airfoil. The NACA 64A0101 airfoil is selected for this calculation because the experimental data is available. The fine mesh zone or the non-deforming part of the mesh is shown in Figure 11. The first grid point adjacent to the wall has the maximum  $y^+ \leq 3.43$

The NACA 64A0101 airfoil is forced in pitch around its quarter chord sinusoidally. The angle of attack is imposed as a function of time as  $\alpha(t) = \alpha_m + \alpha_o \sin(\omega t)$ , where  $\alpha_m$  and  $\alpha_o$  are the mean angle of attack and the amplitude of oscillation respectively. The  $\omega$  is the angular frequency which is directly related to the reduced frequency  $K_c = \frac{\omega c}{2U_\infty}$ , where  $c$  is the airfoil chord, and  $U_\infty$  is the free-stream velocity. To compare with the experimental results given by Davis[32], the primary parameters used in the computation are listed as follows:  $\alpha_m = 0$ ,  $\alpha_o = 1.01^\circ$ ,  $Re = 1.256 \times 10^7$ ,  $M_\infty = 0.8$ , reduced frequency,  $K_c = 0.202$ .

Again, the computation begins with the steady state flow field of the stationary airfoil at 0 degree angle of attack with a dimensionless time step  $\Delta t = 0.1$ . The transition period takes about 3 cycles and the results becomes periodic in time after that. Figure 12 shows the lift oscillation versus the angle of attack after the flow field reaches its temporally periodic solution. The computed lift oscillation agrees well with the experiment[32], which has an evident improvement compared to the recent result computed by McMullen et al. in 2002 [33].

Fig. 13 shows the computed moment coefficient compared with the experiment[32]. The computed moment coefficient does not agree as accurately with the experiment as the lift coefficient does. However the results are very similar to those predicted by Bohbot et al.[10] and McMullen et al.[33]. The large discrepancy between the computation and the experiment for the moment coefficient may be due to the inadequacy of the turbulence modeling, which may not predict the surface friction accurately.

## 5.4 Flow-Induced Vibration of NACA 64A010 Airfoil

The structural model for the flow-induced vibration of a 2-D sweptback wing with a NACA 64A010 cross-section is described in section 3.2. This model was first introduced by Isogai [34] [34], and has been numerically investigated by several researchers [2] [11] [9] [10]. The structural parameters used in this model are listed as the following:  $a = -2.0$ ,  $x_\alpha = 1.8$ ,  $\frac{\omega_\alpha}{\omega_h} = 1$ ,  $r_\alpha^2 = 3.48$ , and  $\mu = 60$ . The elastic axis is located half a chord upstream of the airfoil nose.

The unsteady Reynolds averaged Navier-Stokes equations with the Baldwin-Lomax turbulence model are solved for the flow field in this study. The freestream conditions are:  $Re = 1.256 \times 10^7$ ,  $M_\infty = 0.825$ .

Due to the symmetric profile of the NACA 64A010 airfoil, an initial perturbation is imposed to trigger the oscillating motion. The airfoil is forced to rotate sinusoidally about its elastic axis at the natural frequency in pitch  $\omega_\alpha$  with an angle of attack amplitude,  $\alpha_o = 1^\circ$ . Usually the forced pitching mode lasts for 1 - 3 cycles. After that, the elastically mounted airfoil is let to move in both plunging and pitching directions, and then the dynamic response is recorded.

In present study, the search of the critical point on the transonic flutter boundary at a given *Mach* number is conducted. The speed index,  $V^*$  defined as  $\frac{U^*}{\sqrt{\mu}}$ , is the parameter to classify damped, neutral and divergent responses of the airfoil when the *Mach* is fixed. In this case, the total pressure and temperature need to be adjusted to match the certain value of the *Re* number. Several calculations are needed to determine the critical point using a bi-section method.

In Figures (14) through (16) the time histories of plunging and pitching displacements at  $M_\infty = 0.825$  are plotted for three different  $V^*$ . In these figures, from  $V^* = 0.55$  to  $V^* = 0.70$ , the plots correspond to the damped, neutral, and diverging responses respectively. The major task of calculating a flutter boundary is to locate where the neutrally stable (critical point) is by looking at those plots and determining where the neutral response occurs as the  $V^*$  varies. When the value of  $V^*$  is smaller than the critical value on the flutter boundary, both plunging and pitching displacements decay corresponding to the damped response as shown in Figure (14). Once the value of  $V^*$  coincides with or is close to the critical value, the neutral response appears as shown in Figure (15). Any value of  $V^*$  beyond the critical value, a diverging response is expected as shown in Figure (16). Mach number 0.825 is located at the bottom of the sonic dip as reported in [16, 9, 10]. The predicted critical velocity index  $V^* = 0.615$  is consistent with the results computed by those researchers.

## 6 Conclusion

The efficient high resolution E-CUSP upwind scheme newly suggested by Zha and Hu [23] has been successfully extended and applied to calculate flow induced vibration with moving grid based on fully coupled fluid-structural interaction.

For an elastically mounted cylinder, various cases with different structural parameters have been calculated. The predicted displacement agrees very well with the experiment and the numerical results of other researchers.

For the forced pitching NACA 64A010 airfoil, the computed lift oscillation agrees accurately with the experiment. The computed moment oscillation has large deviation from the experiment, but the results are in the similar accuracy order as other researchers have achieved. The discrepancy may be due to the inaccurate prediction of the surface shear stress caused by the inadequacy of the turbulence modeling.

The same airfoil then has been calculated as an elastically mounted airfoil with flow induced vibration. The computations have been carried out using different values of velocity index  $V^*$  which are below, close, and beyond the critical point on the flutter boundary. The corresponding responses of the airfoil flows are well simulated. The predicted value of  $V^*$  at the bottom of the transonic dip is consistent with the numerical results of other researchers [16, 10, 9].

The E-CUSP scheme of Zha-Hu is proved to be robust, accurate and efficient for calculating flow induced vibrations based on fully coupled fluid-structural interaction.

## 7 Acknowledgment

This work is supported by AFOSR Grant F49620-03-1-0253 monitored by Dr. Fariba Fahroo.

## References

- [1] R. B. Melville and S. A. Morton, "Fully Implicit Aeroelasticity on Oveerset Grid Systems ." AIAA Paper-98-0521, 1998.

- [2] O. Bendiksen and K. Kousen, “Transonic Flutter Analysis Using the Euler Equations.” AIAA Paper 87-0911, 1987.
- [3] G. Guruswamy, “Unsteady Aerodynamic and Aeroelastic Calculations for Wings Using Euler Equations,” *AIAA Journal*, vol. 28, pp. 461–469, March 1990.
- [4] E. Lee-Rausch and J. Batina, “Wing Flutter Computations Using an Aerodynamics Model Based on the Navier-Stokes Equations,” *Journal of Aircraft*, vol. 33, pp. 1139–1147.
- [5] M. Smith, “Flight Loads Prediction Methods for Aircraft: Vol I. Euler/Navier-Stokes Aeroelastic Method (ENS3DAE) Technical Development Summary: Version 4.0.” WRDC-TR-89-3104, 1989.
- [6] S. Vermeersch, P. Raj, R. Weed, and L. Sankar, “Towards Cost-Effective Aeroelastic Analysis on Advanced Parallel Computing Systems .” AIAA Paper 97-0646, 1997.
- [7] S. Darracq, S. Champagneux, and A. Corjon, “Computation of Unsteady Turbulent Airfoil Flows with an Aeroelastic AUSM+ Implicit Solver.” AIAA Paper-98-2411, 1998.
- [8] F. J. Blom and P. Leyland, “Analysis of Fluid-Structure Interaction by Means of Dynamic Unstructured Meshes.” AD-Vol. 53-3, 4th International Symposium on Fluid-Structure Interaction, Aeroelasticity, Flow-Induced Vibrations and Noise, Volume I, ASME, 1997.
- [9] B. B. Prananta, H. M. H. L., and Z. R. J., “Two-Dimensional Transonic Aeroelastic Analysis Using Thin-Layer Navier-Stokes Method,” *Journal of Fluid and Structures*, vol. 12, pp. 655–676, 1998.
- [10] J. Bohbot and D. Darracq, “Time Domain Analysis of Two D.O.F. Airfoil Flutter Using an Euler/Turbulent Navier-Stokes Implicit Solver.” International Forum on Aeroelasticity and Structural Dynamics, Madrid, Spain, June 5-7, 2001.
- [11] J. J. Alonso and A. Jameson, “Fully-Implicit Time-Marching Aeroelastic Solutions.” AIAA Paper 94-0056, 1994.
- [12] J. Alonso, L. Martinelli, and A. Jameson, “Multigrid Unsteady Navier-Stokes Calculations with Aeroelastic Applications.” AIAA Paper 95-0048, 1995.
- [13] S. A. Morton, R. B. Melville, and M. R. Visbal, “Accuracy and Coupling Issues of Aeroelastic Navier-Stokes Solutions on Deforming Meshes.” AIAA Paper-97-1085, 1997.
- [14] R. B. Melville, S. A. Morton, and D. P. Rizzetta, “Implementation of a Fully-Implicit, Aeroelastic Navier-Stokes Solver.” AIAA Paper-97-2039, 1997.
- [15] F. Liu, J. Cai, Y. Zhu, A. Wong, and H. Tsai, “Calculation of Wing Flutter by a Coupled CFD-CSD Method.” AIAA-2000-0907, 2000.
- [16] X.-Y. Chen, G.-C. Zha, and Z.-J. Hu, “Numerical Simulation of Flow Induced Vibration Based on Fully Coupled-Structural Interactions.” AIAA Paper 2004-2240, Juun 28 - July 1, 2004.
- [17] A. Jameson, “Analysis and Design of Numerical Schemes for Gas Dynamics I: Artificial Diffusion, Upwind Biasing, Limiters and Their Effect on Accuracy and Multigrid Convergence in Transonic and Hypersonic Flow.” AIAA Paper 93-3359, July, 1993.



- [18] A. Jameson, “Analysis and Design of Numerical Schemes for Gas Dynamics I: Artificial Diffusion, Upwind Biasing, Limiters and Their Effect on Accuracy and Multigrid Convergence in Transonic and Hypersonic Flow,” *Journal of Computational Fluid Dynamics*, vol. 4, pp. 171–218, 1995.
- [19] A. Jameson, “Analysis and Design of Numerical Schemes for Gas Dynamics II: Artificial Diffusion and Discrete Shock Structure,” *Journal of Computational Fluid Dynamics*, vol. 5, pp. 1–38, 1995.
- [20] D. Hänel, R. Schwane, and G. Seider, “On the Accuracy of Upwind Schemes for the Solution of the Navier-Stokes Equations.” AIAA paper 87-1105 CP, 1987.
- [21] J. R. Edwards, “A Low-Diffusion Flux-Splitting Scheme for Navier-Stokes Calculations.” AIAA Paper 95-1703-CP, June, 1995.
- [22] J. R. Edwards, “A Low-Diffusion Flux-Splitting Scheme for Navier-Stokes Calculations,” *Computer & Fluids*, vol. 6, pp. 635–659, 1997.
- [23] G.-C. Zha and Z.-J. Hu, “Calculation of Transonic Internal Flows Using an Efficient High Resolution Upwind Scheme.” AIAA Journal, Feb. 2004.
- [24] B. Baldwin and H. Lomax, “Thin-Layer Approximation and Algebraic Model for Separated Turbulent flows.” AIAA Paper 78-257, 1978.
- [25] A. Jameson, “Time Dependent Calculations Using Multigrid with Application to Unsteady Flows past Airfoils and Wings.” AIAA Paper 91-1596, 1991.
- [26] A. Roshko, “On the Development of Turbulent Wakes From Vortex Streets.” NACA Rep. 1191, 1954.
- [27] S. Goldstein, “Modern Developments in Fluid Dynamics.” Clarendon Press, Oxford, 1938.
- [28] A. Roshko, “On the Development of Turbulent Wakes From Vortex Streets.” NACA Technical Note 2913, 1953.
- [29] O. Griffin, “Vortex-Induced Vibrations of Marine Structures in Uniform and Sheared Currents.” NSF Workshop on Riser Dynamics, University of Michigan, 1992.
- [30] H. Blackburn and G. Karniadakis, “Two and Three-Dimensional Vortex-Induced Vibration of a Circular Cylinder.” ISOPE-93 Conference, Singapore, 1993.
- [31] P. Cook, M. McDonald, and M. Firmin, “Aerofoil rae 2822 - pressure distributions, and boundary layer and wake measurements. experimental data base for computer program assessment,” Tech. Rep. AGARD Report AR-138, AGARD, 1979.
- [32] S. S. Davis, “Naca 64 a010 (naca ames model) oscillatory pitching,” Tech. Rep. AGARD Report No. 702, AGARD, August 1982.
- [33] M. McMullen, A. Jameson, and J. Alonso, “Application of a Non-Linear Frequency Domain Solver to the Euler and Navier-Stokes Equations.” AIAA Paper-2002-0120, 2002.
- [34] K. Isogai, “Transonic Dip Mechanism of Flutter of a Sweptback Wing: Part II,” *AIAA Journal*, vol. 19, pp. 1240–1242, September 1981.

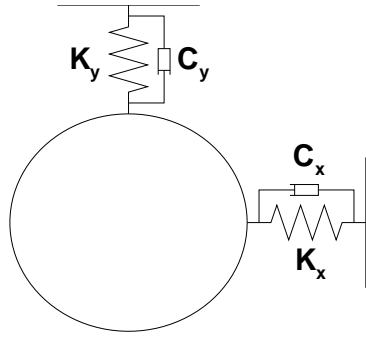


Figure 1: Sketch of the elastically mounted cylinder

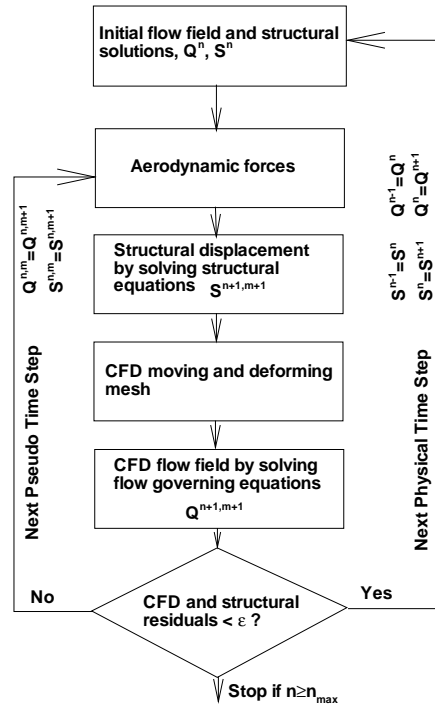


Figure 3: Flow-Structure Interaction Calculation Steps

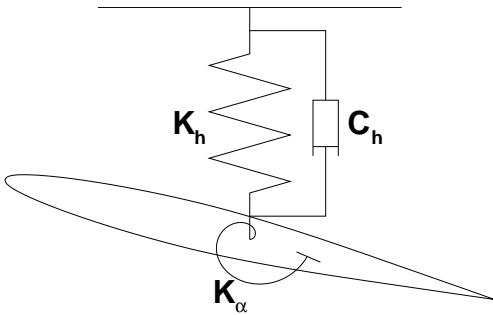


Figure 2: Sketch of the elastically mounted airfoil

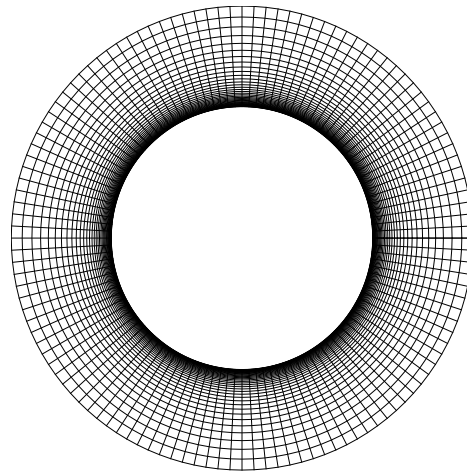


Figure 4: Mesh around the cylinder near the solid surface

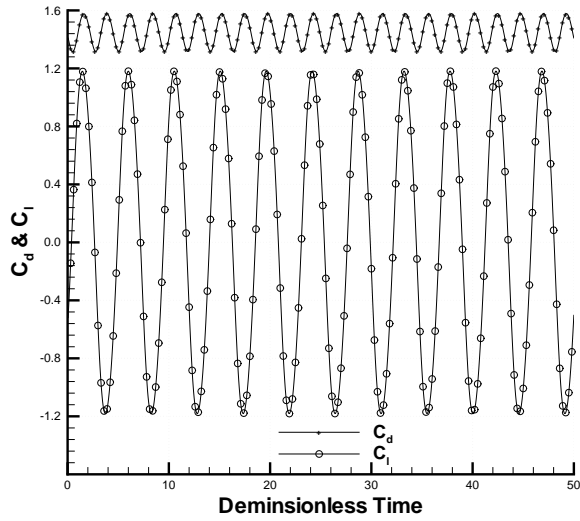


Figure 5: Time history of the lift and drag of the stationary cylinder due to vortex shedding

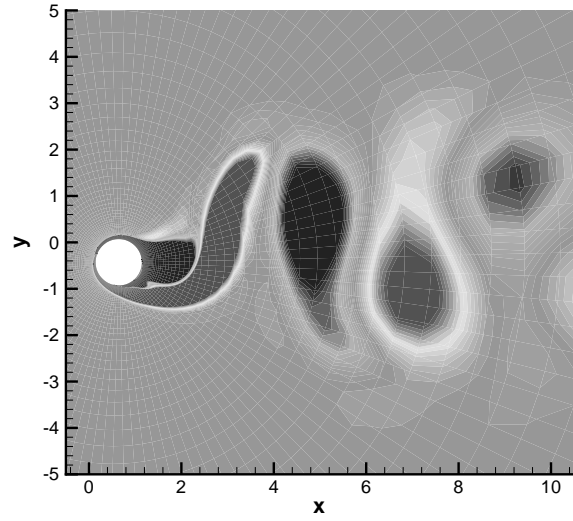


Figure 7: Vorticity contours around oscillating cylinder,  $\mu_s = 1.2732$ ,  $\zeta = 0.03166$ ,

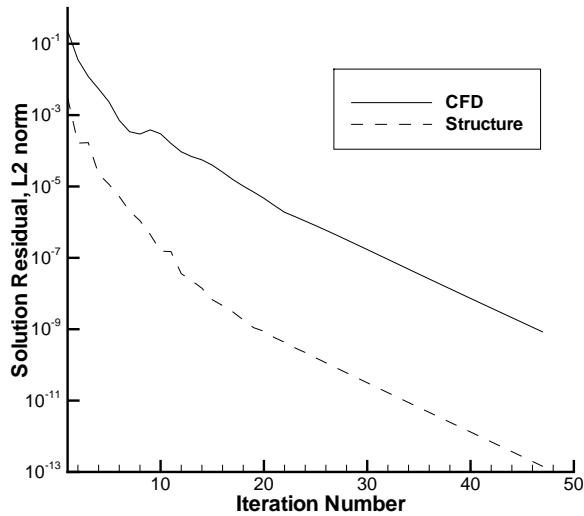


Figure 6: Convergence history of the CFD and structure solver with one physical time step

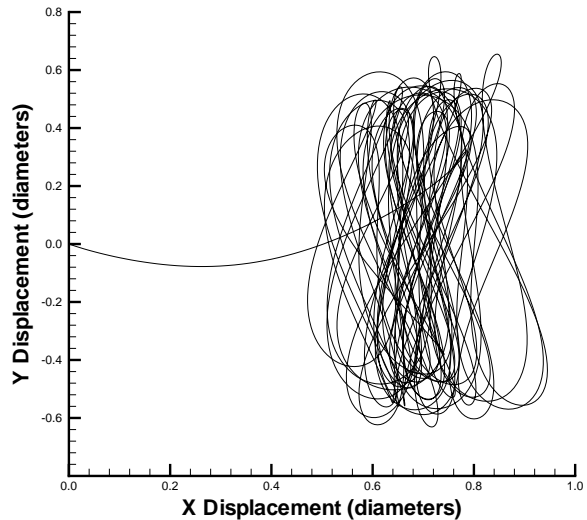


Figure 8: The trajectory of the center of the oscillating cylinder,  $\mu_s = 1.2732$ ,  $\zeta = 0.03166$

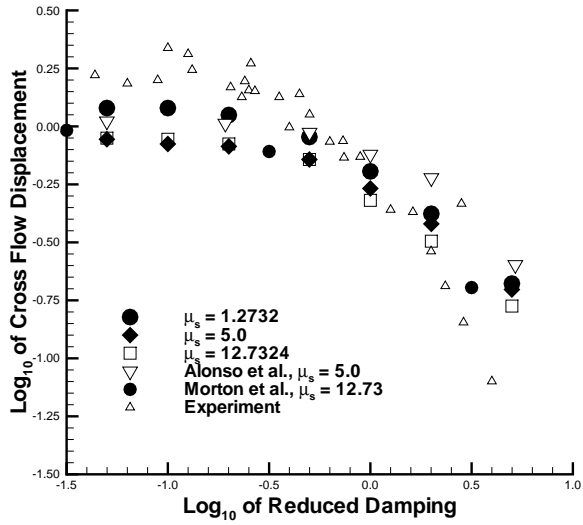


Figure 9: Comparison of the computed amplitude with Griffin's experimental data for the elastically mounted cylinder.

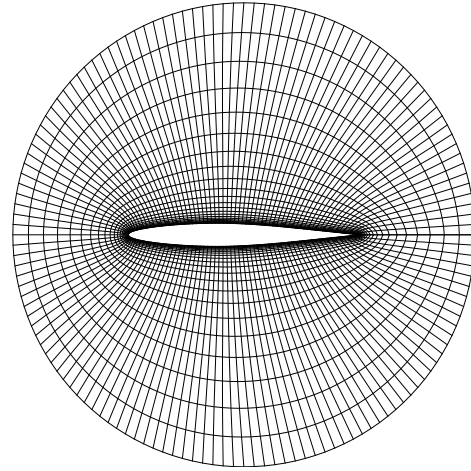


Figure 11: O-type mesh around the NACA 64A010 airfoil

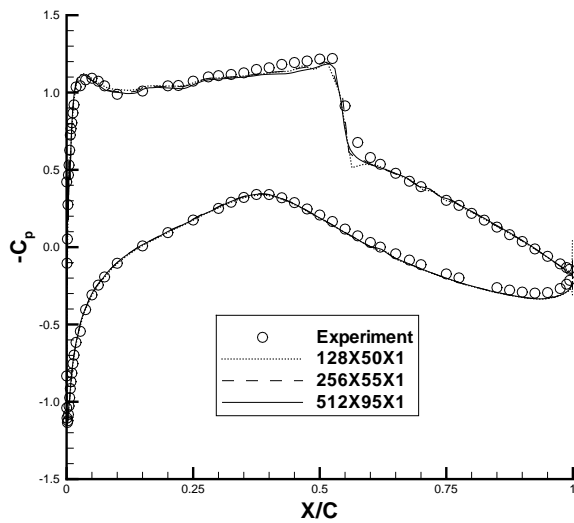


Figure 10: Pressure coefficient comparison

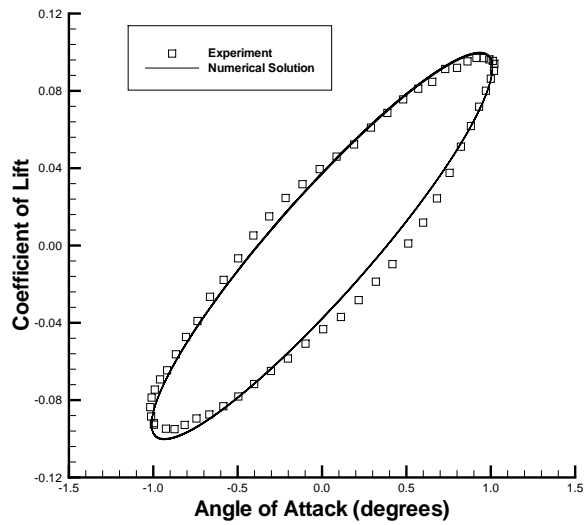


Figure 12: Comparison of computed lift coefficient with Davis' experimental data for the forced pitching airfoil.

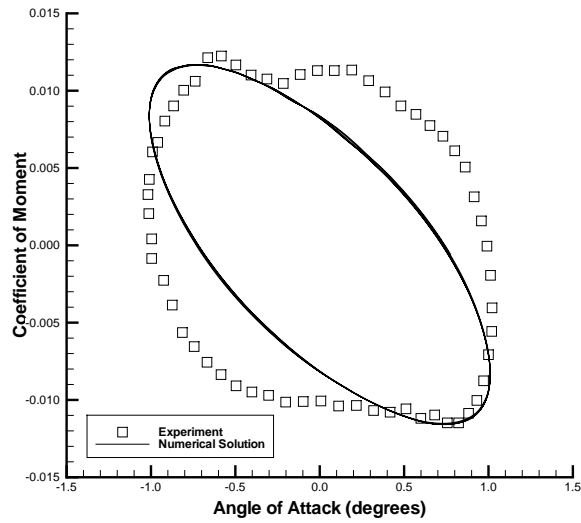


Figure 13: Comparison of computed moment coefficient with Davis' experimental data for the forced pitching airfoil.

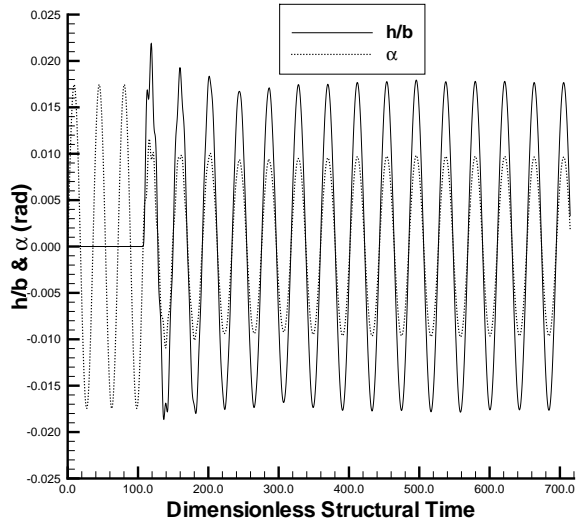


Figure 15: Time histories of plunging and pitching displacements for  $M_\infty = 0.825$  and  $V^* = 0.615$  - Neutrally stable response.

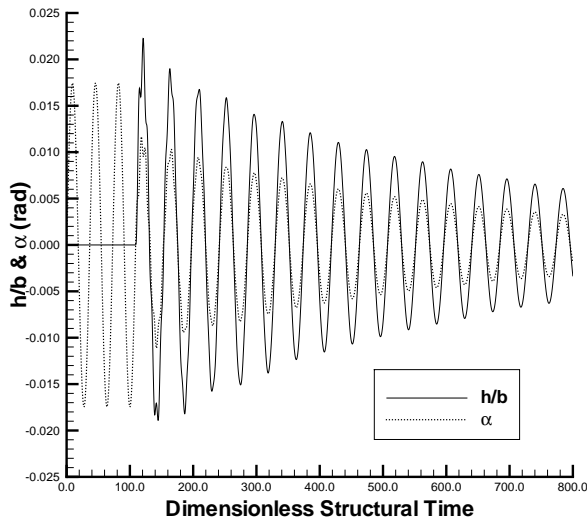


Figure 14: Time histories of plunging and pitching displacements for  $M_\infty = 0.825$  and  $V^* = 0.55$  - Damped response.

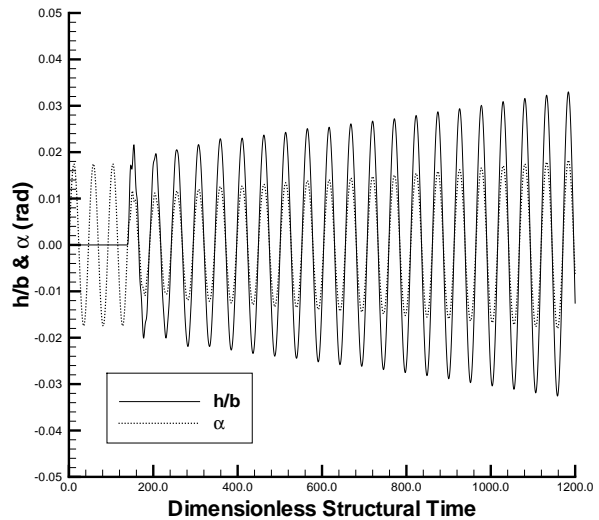


Figure 16: Time histories of plunging and pitching displacements for  $M_\infty = 0.825$  and  $V^* = 0.70$  - Diverging response.